A 3D Framework to Explore the Propagation Effects in Stars Exhibiting Electron Cyclotron Maser Emission

Barnali Das [ORCID], Surajit Mondal [ORCID], and Poonam Chandra [ORCID]
National Centre for Radio Astrophysics, Tata Institute of Fundamental Research, Pune University Campus, Pune-411007, India; barnali@ncra.tifr.res.in
Received 2020 May 20; revised 2020 July 8; accepted 2020 July 13; published 2020 September 11

Abstract

Recently, coherent radio emission has been discovered from a number of hot magnetic stars, via the process of electron cyclotron maser emission (ECME). This emission, observed in the form of highly circularly polarized pulses, has interesting properties that contain information about the host star. One of the important properties of ECME is the frequency dependence of the pulse arrival time. This has been attributed to the propagation effect by Trigilio et al. and could explain the sequence observed for CU Vir qualitatively. However, no quantitative treatment exists for this phenomenon despite it being a promising tool to estimate the density in the stellar magnetosphere. Additionally, the effect of propagation through the magnetosphere on ECME has been thought to be limited to giving rise to a particular sequence of arrival of pulses, and in some cases producing the upper cutoff frequency for ECME. Here, we present a framework to deal with the propagation effect by considering continuous refraction in the inner magnetosphere of the star. This framework is capable of incorporating any type of density distribution, and in principle any type of magnetic field, though we limit ourselves to a dipolar magnetic field for this work. We show by simulation that for stars with high obliquity, the propagation effect can influence not only the sequence of arrival of pulses drastically, but also the pulse shapes, and the observability of a pulse from a particular magnetosphere.

Unified Astronomy Thesaurus concepts: Early-type variable stars (432); Magnetic stars (995); Astronomical simulations (1857); Astrophysical masers (103)

1. Introduction

Coherent radio emission via Electron Cyclotron Maser Emission (ECME) has been observed from a small number of hot magnetic stars (e.g., Trigilio et al. 2000), brown dwarfs (e.g., Hallinan et al. 2006) and planets (e.g., Zarka 1998). The observable signatures of this emission include high brightness temperature, high directivity, and a high degree of circular polarization. Since the presence of a magnetic field is a prerequisite for the ECME phenomenon, discovery of ECME from cold brown dwarfs has led to a surprising revelation that such stars can harbor kilogauss strength magnetic fields (Hallinan et al. 2006, 2008).

In the case of hot magnetic stars, the magnetic fields are already well measured using spectropolarimetry and Zeeman Doppler Imaging (e.g., Kochukhov et al. 2014) revealing the dipole like nature of the magnetic field in most cases. However, there are a few other properties of ECME that can be exploited to study the properties of the host star. For example, the high directivity of the ECME has been used to diagnose the rotation period evolution of the star (Trigilio et al. 2008, 2011); and its magnetoionic mode has been used to estimate the plasma density at the site of emission (Leto et al. 2019). However, one aspect of ECME that has not been exploited is that the high directivity of the phenomenon makes it a sensitive probe of the local density structures it passes through.

In a hot massive star, the interaction between the radiatively driven stellar wind and the magnetic field gives rise to a magnetosphere, which is divided into three parts (Andre et al. 1988; Trigilio et al. 2004): an inner magnetosphere, where the magnetic energy dominates over the wind kinetic energy and the magnetic field lines are closed; an outer magnetosphere, where the wind dominates over the magnetic field; and a middle magnetosphere, the transition region between the inner

and the outer magnetospheres. The middle magnetosphere is the origin of radio emission, including gyrosynchrotron emission and the ECME. The boundary of the inner magnetosphere, at which the magnetic field energy equals the wind kinetic energy, is called the Alfvén surface. The inner magnetosphere (hereafter IM) is the densest part of the magnetosphere, with the largest imprints on the ECME lightcurves. In this paper, we present a framework to understand the effect of refraction on the ECME lightcurves while passing through the stellar magnetosphere. This, in turn, will allow us to acquire information about the density structure in the stellar magnetosphere. This framework is valid for any arbitrary density distribution and in principle for any type of arbitrary magnetic field; however, we confine ourselves to a dipolar magnetic field in this paper.

This paper is structured as follows. In the next section, we present a brief summary of ECME observed from magnetic AB stars (Section 2). We present our framework in Section 3, followed by a few examples of its application in Section 4. We end this paper with a discussion in Section 5.

2. ECME from a Star with an Axisymmetric Dipolar Magnetic Field

The expected ECME lightcurve from a star with an axisymmetric dipolar magnetic field consists of two pairs of pulses, each pair consisting of one left circularly polarized (LCP) and one right circularly polarized (RCP) pulse coming from opposite magnetic hemispheres (Leto et al. 2016). The LCP and RCP pulses for a given pair lie symmetrically around a magnetic null phase, which is the rotational phase where the line-of-sight (LoS) component of the magnetic field is zero (B_{LoS}). There are two such rotational phases per stellar rotation cycle for a dipolar magnetic field, corresponding to two pairs of

ECME pulses. The sequence of arrival of the RCP and LCP pulses is opposite near the two nulls. Around the null where B_{LoS} is changing from positive to negative, the pulse from the northern magnetic hemisphere will arrive first, followed by the one from the southern magnetic hemisphere. Around the other null, where B_{LoS} is changing from negative to positive, the pulse from the southern magnetic hemisphere will arrive before the one from the northern magnetic hemisphere (Leto et al. 2016). This is a consequence of the fact that due to refraction, the pulse from the northern magnetic hemisphere deviates upward, and the one from the south deviates downward (Trigilio et al. 2011; Leto et al. 2016). Note that this picture assumes single refraction at the boundary between the middle and the inner magnetosphere at the time the latter is entered. In reality, we often see a more complicated sequence of arrival of pulses (Das et al. 2019a, 2019b). Moreover, the pulses are almost never seen to lie symmetrically about the magnetic null phases (Das et al. 2019a, 2019b; Leto et al. 2019). We will show subsequently that at least some of these features can be explained by propagation effects alone.

3. The Framework

To date, not many studies have attempted to understand the effects of the refraction experienced by ECME pulses while traveling through the stellar magnetosphere on their way to the observer. The importance of refraction was first realized by Trigilio et al. (2011), who proposed it to be the cause of the difference in pulse arrival time at two different frequencies in CU Vir, the first known hot magnetic star with ECME (Trigilio et al. 2000). They attributed it to the different amounts of deviation suffered due to the refraction in a cold torus with a constant plasma density of $10^9 \, \mathrm{cm}^{-3}$ (taken from the simulation of Leto et al. 2006) near the magnetic equator. While doing that, they considered the refraction effect only at the time the pulse entered the cold torus. This scenario was later shown by Lo et al. (2012) to correctly reproduce the pulse arrival sequence of the ECME from CU Vir at 13 cm and 20 cm; however, the amount of "lag" (difference in rotational phases of arrival for the two frequencies) between the two pulses could not be reproduced.

Here we propose a general framework that will enable the effect of propagation on the ECME lightcurves for any arbitrary density distribution in the IM to be studied. We use the model proposed by Trigilio et al. (2011) for the emission of ECME. According to this model, the pulses are emitted tangential to the auroral rings such that they are perpendicular to the local magnetic field vector and parallel to the magnetic equatorial plane (Figure 1).

We divide the whole problem into three parts:

1. Determine the initial condition, i.e., the ray direction immediately after entering the IM for a given point of origin of the radiation on the auroral circle.
2. Solve the ray path inside the IM.
3. Find out the ray direction after exiting the IM.

We assume that the density in the middle and the outer magnetosphere is low enough that the refractive indices are unity outside the IM. Before presenting our framework in the next section, we would like to clarify that the division of the stellar magnetosphere into three discontinuous parts (inner, middle, and outer) is a highly simplified description. In reality, the transition from one region to another is much more
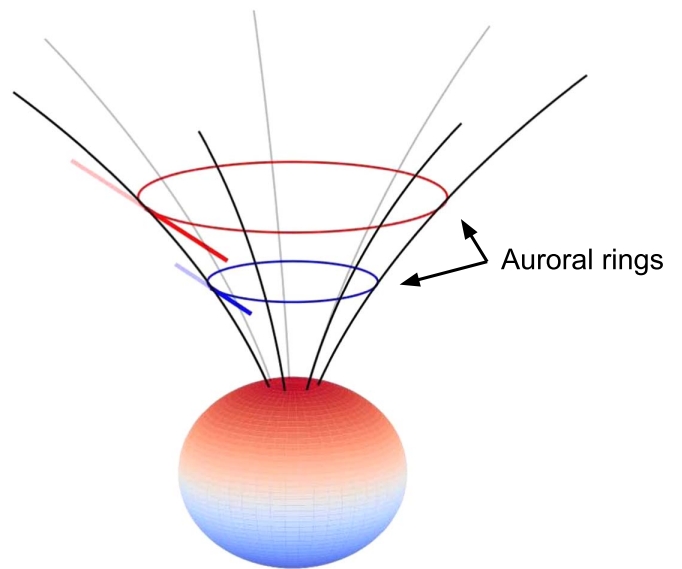

Figure 1. The "tangent plane beaming model" for ECME proposed by Trigilio et al. (2011). ECME is produced tangential to the auroral rings such that the direction is perpendicular to the local magnetic field and parallel to the magnetic equatorial plane. Lower frequencies originate farther away from the star and vice versa.
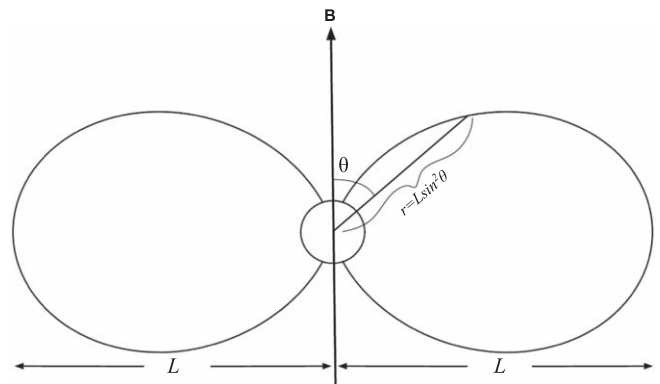

Figure 2. The closed magnetic field lines around a star (drawn as the central circle) with a dipolar magnetic field. The axis of the dipole is shown as the vertical arrow and the polar strength on the stellar surface is B. The equation of a field line in polar coordinates is $r = L \sin^2 \theta$, where r is measured from the center of the star and θ is measured from the dipole axis. L is the maximum value of r along that field line, which is obtained for $\theta = 90°$, i.e., at the magnetic equator. The IM contains field lines with $L \leqslant R_A$.

complex, as demonstrated in various MHD simulations of hot magnetic stars (e.g., Townsend et al. 2007; Ud-Doula et al. 2008; ud-Doula et al. 2013, etc.).

3.1. The Initial Condition

In the frame of reference of the magnetic field, we choose the Z-axis to lie along the dipole axis. The X- and Y-axes are arbitrary at this point, but will be defined later (Section B). The magnetic field lines in polar coordinates are given by $r = L \sin^2 \theta$ (Figure 2). The IM is bounded by the field line $r = R_A \sin^2 \theta$, where R_A is the Alfvén radius for the star; the field lines inside IM have $L < R_A$, and those outside have $L > R_A$.

Let the frequency of the ECME be ν, which is related to the local magnetic field strength B as $\nu \approx s \times 2.8B$ (ν is in MHz and B is in G), where s is the harmonic number. In other words,
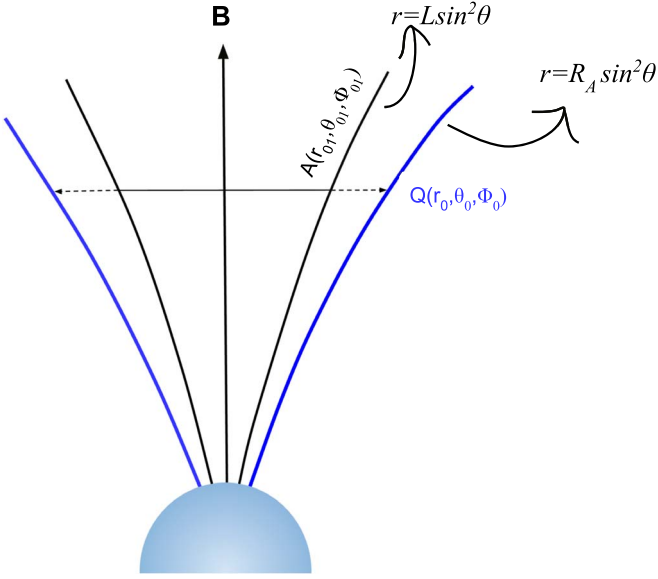
Figure 3. A cartoon diagram showing ECME produced at point A that hits the inner magnetosphere boundary at point Q.

the ECME at a frequency ν will be produced at those points in the middle magnetosphere, at which the magnetic field strength is $B = \nu/(2.8s)$. For a dipolar magnetic field, these points constitute a (auroral) circle above each magnetic pole (Figure 1) around magnetic field lines given by $r = L \sin^2 \theta$. Each point on this auroral circle is a source of the ECME. We consider one such point $A(r_{01}, \theta_{01}, \phi_{01})$ (Figure 3). If the polar magnetic field on the stellar surface is B_0, we have

$$\boldsymbol{B} = \frac{B_0}{r_{01}^3}\left(\cos\theta_{01}\hat{r} + \frac{1}{2}\sin\theta_{01}\hat{\theta}\right)$$

$$\Rightarrow B = \frac{B_0}{L^3 \sin^6 \theta_{01}}\sqrt{1 - \frac{3}{4}\sin^2\theta_{01}}$$

$$\therefore L^3\frac{B}{B_0} - \frac{1}{\sin^6\theta_{01}}\sqrt{1 - \frac{3}{4}\sin^2\theta_{01}} = 0, \qquad (1)$$

where we have used $r_{01} = L \sin^2\theta_{01}$. By solving this equation, we will get θ_{01} and subsequently r_{01}.

To get the direction of the wavevector ($\boldsymbol{k}$) at the point A, immediately after emission, we use the fact that $\boldsymbol{k}$ is perpendicular to both the dipole axis and the local magnetic field $\boldsymbol{B}$ at the point $A(r_{01}, \theta_{01}, \phi_{01})$. The first condition implies that $\boldsymbol{k}$ lies in the XY plane. The second condition implies that

$$\boldsymbol{k} \cdot \boldsymbol{B} = 0$$
$$k_x B_x + k_y B_y = 0$$
$$\therefore \frac{k_x}{k_y} = -\frac{B_y}{B_x}. \qquad (2)$$

This equation gives two possible directions of the wavevector at the given point A that are antiparallel to each other.

The next task is to find the point $Q(r_0, \theta_0, \phi_0)$ where the ray will hit the boundary of the IM (Figure 3). As we have assumed that the refractive index in the middle magnetosphere is unity, the direction of the wavevector $\boldsymbol{k}$ will not change while traveling from points A to Q. Since $\boldsymbol{k}$ has no z component, we must have the z coordinate of point Q be the same as that of
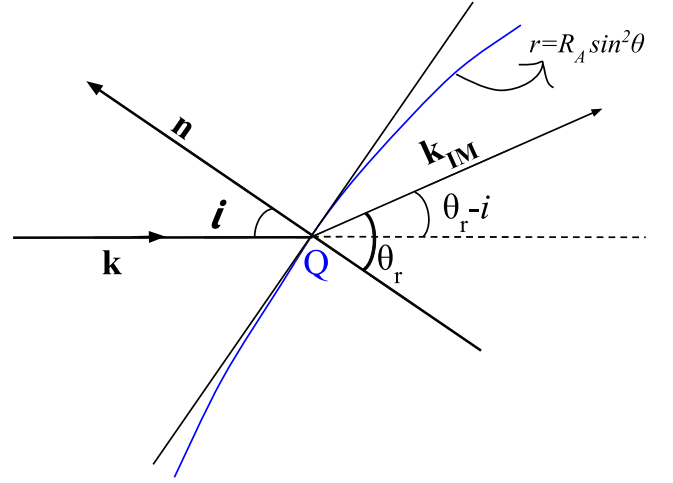

Figure 4. The direction of the wavevector $\boldsymbol{k}_{\mathrm{IM}}$ immediately after entering the inner magnetosphere and its relation with the incident wavevector $\boldsymbol{k}$ and the normal to the surface $\boldsymbol{n}$.

point A. Thus, we have

$$(R_A \sin^2\theta_0)\cos\theta_0 = r_{01}\cos\theta_{01}.$$

By solving this equation, θ_0 can be found. We can then obtain r_0 using $r_0 = R_A \sin^2\theta_0$.

To determine ϕ_0, we use the fact that the vector connecting points Q and A must be parallel to $\boldsymbol{k}$, i.e.,

$$\frac{r_0 \sin\theta_0 \cos\phi_0 - r_{01}\sin\theta_{01}\cos\phi_{01}}{r_0 \sin\theta_0 \sin\phi_0 - r_{01}\sin\theta_{01}\sin\phi_{01}} = \frac{k_x}{k_y}. \qquad (3)$$

Now we require the angle of incidence at point Q. For that we determine the normal ($\hat{n}$) to the IM boundary, which is given by the gradient to the surface at that point. The angle of incidence is then given by $i = \pi - \cos^{-1}(\hat{n} \cdot \hat{k})$ (Figure 4).

We now determine the angle of refraction. As already mentioned above, the refractive index outside the IM (μ_1) is assumed to be unity and that inside the IM (μ_2) can be calculated using the density model of the IM. One caveat here is that μ_2 depends not only on the plasma density, but also on the angle between the wavevector and the magnetic field vector immediately inside the IM (Equation (A1)). It is not possible to know the direction of the wavevector inside the IM beforehand. This difficulty can be overcome by adopting an iterative approach. We first calculate the value of μ_2 using the same value for the angle between the wavevector and the magnetic field as that before entering the IM. Using the angle of incidence (i), μ_1, and μ_2, the angle of refraction θ_r can be found from Snell's law. To find the direction of the wavevector just after entering the IM ($\boldsymbol{k}_{\mathrm{IM}}$), we note that

$$\boldsymbol{k}_{\mathrm{IM}} \propto \hat{r} + r\theta'\hat{\theta} + r\sin\theta\phi'\hat{\phi}. \qquad (4)$$

For obtaining the ray path, we are interested only in the direction of $\boldsymbol{k}_{\mathrm{IM}}$. Hence we set $\boldsymbol{k}_{\mathrm{IM}} = \gamma(\hat{r} + r\theta'\hat{\theta} + r\sin\theta\phi'\hat{\phi})$, where $\gamma = \pm 1$. We already know the values of r, θ, and ϕ at point Q, which are respectively r_0, θ_0, and ϕ_0. To find $\theta' = d\theta/dr$ and $\phi' = d\phi/dr$ at point (r_0, θ_0, ϕ_0) inside the

IM, we solve the following two equations (Figure 4):

$$\hat{k} \cdot \boldsymbol{k}_{\mathrm{IM}} = |\boldsymbol{k}_{\mathrm{IM}}| \cos(\theta_r - i)$$
$$\hat{n} \cdot \boldsymbol{k}_{\mathrm{IM}} = |\boldsymbol{k}_{\mathrm{IM}}| \cos(\pi - \theta_r).$$

By solving these two equations, we can find θ'_0 and ϕ'_0 immediately after entering the IM. Once the new direction of the wavevector is known, we can find the angle made by it with the local magnetic field vector. This in turn is used to calculate μ_2 to get an improvement over the previous estimation. This cycle is continued until we achieve convergence. θ'_0 and ϕ'_0 are then calculated using the value of μ_2 obtained after convergence.

The five values: r_0, θ_0, ϕ_0, θ'_0, and ϕ'_0 will serve as the initial conditions required to solve the ray path inside the IM.

3.2. Ray Path Inside the Inner Magnetosphere

To find the ray path inside the IM, we use the Fermat's principle (Wolin 1953). According to this principle, the path is given by the minimization of $\int \mu ds$ (note that $\mu = \mu_2$ at the point Q inside the IM). Now

$$ds = \sqrt{dr^2 + r^2 d\theta^2 + r^2 \sin^2\theta d\phi^2}$$
$$= dr\sqrt{1 + r^2\theta'^2 + r^2 \sin^2\theta\phi'^2}$$
$$= G \times dr,$$

where $G = \sqrt{1 + r^2\theta'^2 + r^2 \sin^2\theta\phi'^2}$. Let,

$$F(r, \theta, \phi, \theta', \phi') = \mu \times G.$$

To minimize F, we use the Euler-Lagrange equation that gives:

$$\frac{\partial F}{\partial \theta} - \frac{d}{dr}\frac{\partial F}{\partial \theta'} = 0, \tag{5}$$

$$\frac{\partial F}{\partial \phi} - \frac{d}{dr}\frac{\partial F}{\partial \phi'} = 0. \tag{6}$$

By integrating this equation numerically, we can find the ray path $\{\theta(r), \phi(r)\}$ inside the IM. To do that, we cast the above equations in the following form:

$$\frac{dY_1}{dr} = \frac{\partial F}{\partial \theta}, \quad \frac{dY_2}{dr} = \frac{\partial F}{\partial \phi}$$
$$Y_1 = \frac{\partial F}{\partial \theta'}, \quad Y_2 = \frac{\partial F}{\partial \phi'}.$$

We assume the step size of the integration (in r) to be Δr. Then, at step i, we have

$$r_{i+1} = r_i + \Delta r$$
$$\theta_{i+1} = \theta_i + \theta'_i \Delta r$$
$$\phi_{i+1} = \phi_i + \phi'_i \Delta r$$
$$Y_{1,i+1} = Y_{1,i} + \frac{dY_1}{dr}\bigg|_i \Delta r$$
$$Y_{2,i+1} = Y_{2,i} + \frac{dY_2}{dr}\bigg|_i \Delta r.$$

To obtain θ'_{i+1} and ϕ'_{i+1}, we minimize the following equations:

$$Y_{1,i+1} - \left(\frac{\partial F}{\partial \theta'}\right)_{i+1} = 0, \quad Y_{2,i+1} - \left(\frac{\partial F}{\partial \phi'}\right)_{i+1} = 0.$$
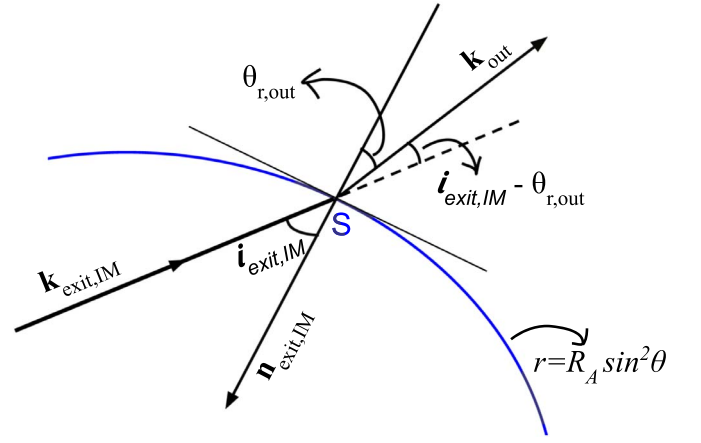

Figure 5. The relation between the direction of the wavevector after entering the IM (k_{out}), the direction of the wavevector just inside the IM ($k_{\mathrm{exit,IM}}$), and the direction of the normal to the boundary of the inner magnetosphere ($n_{\mathrm{exit,IM}}$).

Once we find θ'_{i+1} and ϕ'_{i+1}, we can obtain $(dY_1/dr)_{i+1}$ and $(dY_2/dr)_{i+1}$ in the following way:

$$\frac{dY_1}{dr}\bigg|_{i+1} = \left(\frac{\partial F}{\partial \theta}\right)_{i+1}, \quad \frac{dY_2}{dr}\bigg|_{i+1} = \left(\frac{\partial F}{\partial \phi}\right)_{i+1}.$$

We stop the integration when we achieve the condition $r/\sin^2\theta \geqslant R_{\mathrm{A}}$.

3.3. Ray Direction after Exiting the IM

Let the point at which the ray exits the IM be $S(r_{\mathrm{exit,IM}}, \theta_{\mathrm{exit,IM}}, \phi_{\mathrm{exit,IM}})$ (Figure 5). Let the value of θ' and ϕ' inside the IM at point S be $\theta'_{\mathrm{exit,IM}}$ and $\phi'_{\mathrm{exit,IM}}$, respectively. Using these values, we can readily obtain the direction of the wavevector inside the IM at the exit point $\hat{k}_{\mathrm{exit,IM}}$ (Equation (4)). To find out the wavevector direction after exiting the IM $\hat{k}_{\mathrm{out}}$, we need the angle of refraction. This can be found out using a procedure similar to the one adopted to find the angle of refraction at the time of entering the IM (described in Section 3.1). $\hat{k}_{\mathrm{out}}$ can then be found by solving the following two equations:

$$\hat{k}_{\mathrm{exit,IM}} \cdot \hat{k}_{\mathrm{out}} = \cos(i_{\mathrm{exit,IM}} - \theta_{\mathrm{r,out}})$$
$$\hat{n}_{\mathrm{exit,IM}} \cdot \hat{k}_{\mathrm{out}} = \cos(\pi - \theta_{\mathrm{r,out}})$$

where $i_{\mathrm{exit,IM}}$ and $\theta_{\mathrm{r,out}}$ are respectively the angle of incidence and angle of refraction at point S, and $\hat{n}_{\mathrm{exit,IM}}$ is the inward normal to the IM at point S.

4. Application of the Model

In this section, we demonstrate the applicability of this framework to studying the various properties of the ECME. We consider two kinds of density distributions in the IM: the first is the case of an azimuthally symmetric density distribution in the IM, and the second is the case of an azimuthally asymmetric density distribution in the IM. For the simulation presented here, the step size was determined in an ad hoc manner in which we varied the step size of integration until we got no significant change in the results with a further decrease in the step size. For practical purposes, we recommend using adaptive step size, which can be obtained by determining the length
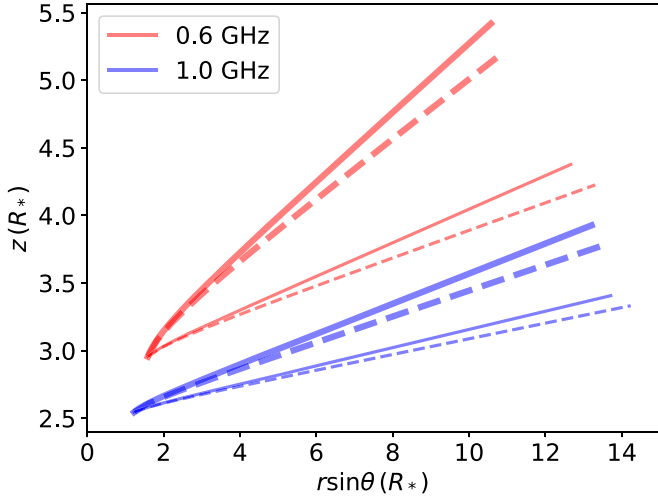
Figure 6. Ray paths inside the inner magnetosphere (IM) generated by our code (solid lines) and those obtained by assuming single refraction at the boundary between inner and middle magnetosphere (dashed lines). The thick and thin lines are respectively for extraordinary (X-) and ordinary (O-) modes of emission at the second harmonic. We have assumed a radially decreasing density profile inside IM given by $n_p = n_{p0}/r$, where $n_{p0} = 10^9$ cm^{-3}. The values of the other parameters used here are $B_0 = 4$ kG, $R_A = 15.0$ and $L = 18.0$. All the distances are in units of stellar radius.
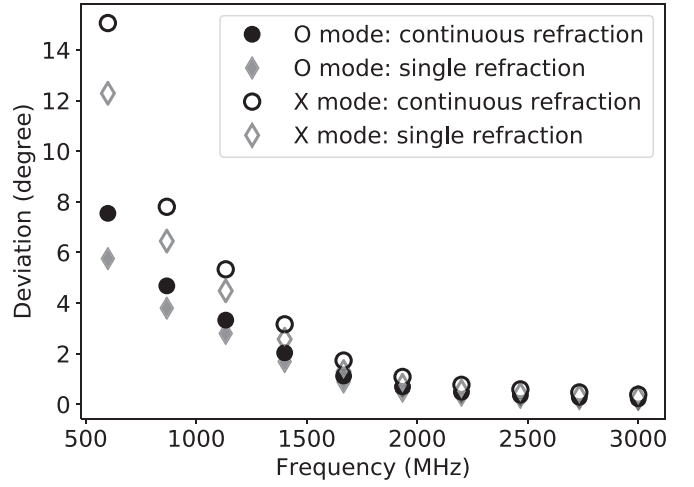

Figure 7. Deviation of the ECME after exiting the IM w.r.t. the initial direction of emission vs. frequency of the radiation. The circles correspond to the deviations obtained from our code, and the diamonds correspond to the deviations obtained by considering single refraction only. The values of the other parameters are the same as those in Figure 6.

scale of the change in the number density at a given point in the IM.

4.1. ECME from a Star with an Azimuthally Symmetric Magnetosphere

We consider a star with an axisymmetric dipolar magnetic field. The star has an inclination angle of $46°.5$ and obliquity of $76°$ (close to the values for CU Vir). We assume that the density inside the IM is $n_p = n_{p0}/r$, where r is the distance in the units of stellar radius from the center of the star and n_{p0} is a normalization constant with $n \to n_{p0}$ as $r \to 1$ (expected from stellar rotation, Leto et al. 2006). We also assume that the ECME is produced at the second harmonic, i.e., $s = 2$. For this type of distribution, the ECME emitted at each point of a given auroral circle experiences identical densities and follows identical paths, such that none of the observable properties of ECME have any dependence on the magnetic azimuthal coordinate ϕ (hereafter ϕ_B).

To calculate the ray paths for the ECME, we assume $n_{p0} = 10^9$ cm^{-3} and $R_A = 15 R_*$, where R_* is the stellar radius. We also assume that the ECME is produced in the auroral rings comprised of magnetic field lines with equatorial radius $L = 18 R_*$. We show the results of our simulation at two frequencies, 0.6 GHz and 1 GHz, in Figure 6. We compare our results with the ones obtained by considering a single refraction at the boundary between the middle and the inner magnetosphere (dashed lines), per the framework of Lo et al. (2012). We carry out simulations for both extraordinary (X-) and ordinary (O-) modes. We find that although the single refraction approach can produce a qualitative picture quite nicely, this underestimates the deviation suffered by the ray. For example, both indicate that the lower frequency deviates more than the higher frequency at a given magnetoionic mode; and at a given frequency, radiation at the X-mode deviates more than that at the O-mode. This is more evident in Figure 7, where we plot the deviation angle (defined as $\theta_D = \pi/2 - \cos^{-1}(\hat{k}_{\rm out} \cdot \hat{z})$, i.e., the angle made by the ray

direction after exiting the IM with the magnetic equatorial plane) versus the frequency of the radiation. We see that as the frequency of the radiation increases, the deviation suffered decreases, and also the difference in the deviation obtained from our code and that obtained by assuming single refraction at the time of entering the IM decreases. This is expected because as we go to higher frequencies (i.e., going closer to the star), the ratio ν_p/ν (ν_p is the plasma frequency) becomes smaller. Note that this phenomenon of ν_p/ν decreasing with decreasing r is a consequence of the assumed density profile, for which $\nu_p \propto 1/\sqrt{r}$, whereas $\nu \propto \nu_B \propto 1/r^3$ (ν_B is the electron gyrofrequency at the site of emission) such that $\nu_p/\nu \propto r^{2.5}$.

From the point of view of an observer, the ray paths are not directly measurable. We need a quantity that is directly measurable from observations and then can be compared with the values predicted by a model. One such quantity is the difference in rotational phases of arrival of pulse at different frequencies (we refer to this quantity as "lag"). For our simple density profile, after obtaining $\hat{k}_{\rm out}$ for any ϕ_{01} (Section 3.3), we can obtain the deviation angle, which we define as $\theta_D = \pi/2 - \cos^{-1}(\hat{k}_{\rm out} \cdot \hat{z})$. Here $\pi/2$ is the angle between the dipole axis and the original direction of emission and $\cos^{-1}(\hat{k}_{\rm out} \cdot \hat{z})$ is the angle between the dipole axis and the direction of the radiation after exiting the IM. This angle is related to the rotational phase $\phi_{\rm rot}$ through the following relation (Trigilio et al. 2000):

$$\sin \theta_D = \sin \beta \sin \alpha \cos 2\pi(\phi_{\rm rot} - \phi_{\rm rot,0}) + \cos \beta \cos \alpha$$

$$\Rightarrow \phi_{\rm rot} - \phi_{\rm rot,0} = \frac{1}{2\pi} \cos^{-1}\left(\frac{\sin \theta_D - \cos \beta \cos \alpha}{\sin \beta \sin \alpha}\right) \quad (7)$$

where α and β are the inclination angle and the angle between the rotation axis and magnetic axis, respectively, and $\phi_{\rm rot,0}$ is the reference rotational phase (which corresponds to the rotational phase when the LoS component of the magnetic field is at maximum). Let the two frequencies be ν_1 and ν_2. The rotational phases of arrival are $\phi_{\rm rot,1}$ and $\phi_{\rm rot,2}$, respectively, and
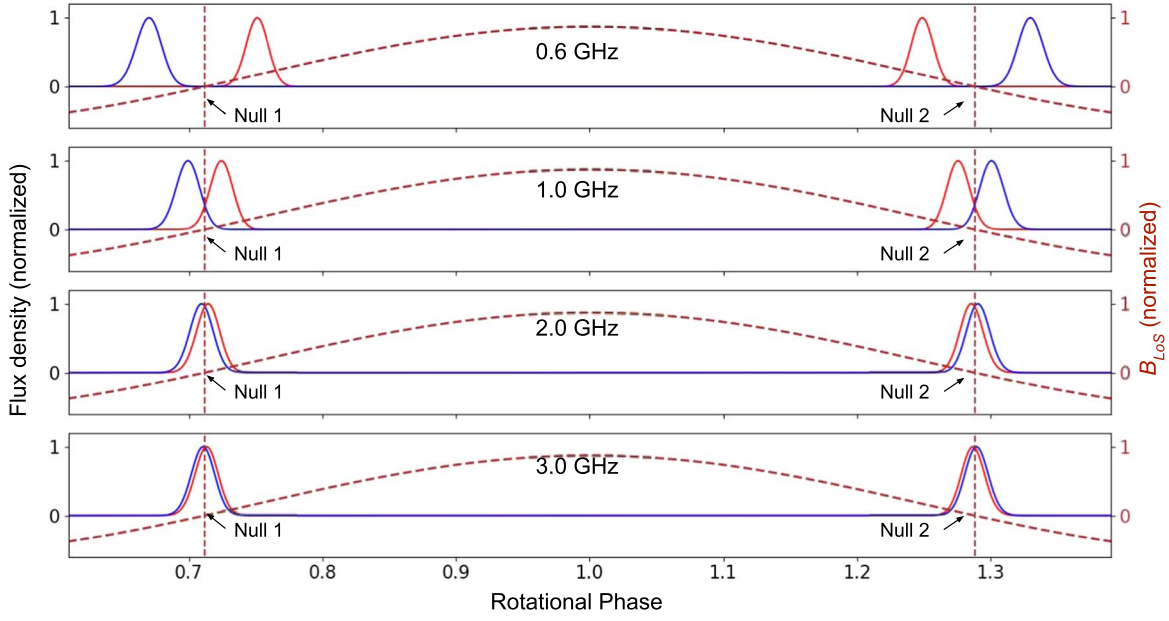
Figure 8. The normalized lightcurves for ECME at 1 GHz, 2 GHz, and 3 GHz, emitted at the second harmonic in the extraordinary mode. The red and blue correspond to ECME produced at the north and south magnetic hemispheres, respectively. The density profile in the IM is given by $n_p = n_{p0}/r$, where $n_{p0} = 10^9$ cm^{-1}. We have used $\sigma_\theta = 3°$ (Section C). We also show the normalized LoS component of the stellar magnetic field ($B_{\rm LoS}$, brown dashed curve). We have used a polar magnetic field strength of 4 kG, inclination angle of 46°5, and obliquity of 76°.
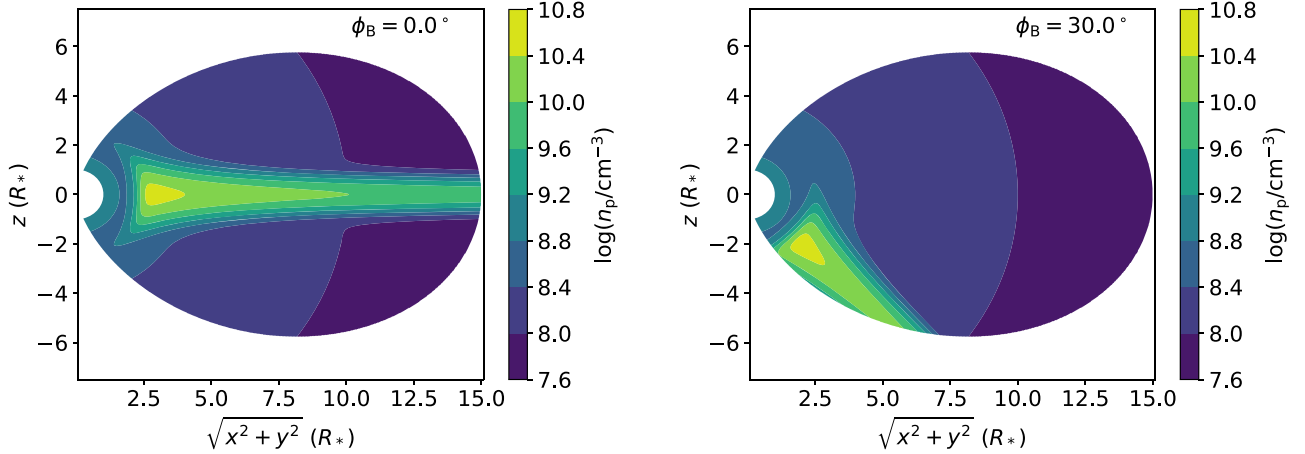
Figure 9. The density profile given by Equation (9) for two different values of the magnetic azimuthal coordinate $\phi_{\rm B}$.

$\phi_{\rm rot,2} - \phi_{\rm rot,1} = \Delta\phi_{\rm rot}$. From Equation (7):

$$\Delta\phi_{\rm rot} = (\phi_{\rm rot,2} - \phi_{\rm rot,0}) - (\phi_{\rm rot,1} - \phi_{\rm rot,0})$$
$$= \frac{1}{2\pi}\cos^{-1}\left(\frac{\sin\theta_{D2} - \cos\beta\cos\alpha}{\sin\beta\sin\alpha}\right)$$
$$- \frac{1}{2\pi}\cos^{-1}\left(\frac{\sin\theta_{D1} - \cos\beta\cos\alpha}{\sin\beta\sin\alpha}\right). \quad (8)$$

Thus from the calculated θ_Ds for a pair of frequencies, the corresponding lag ($=\Delta\phi_{\rm rot}$) can be obtained from Equation (8) and compared to observations.

We end this subsection by showing the X-mode ECME lightcurves at four different frequencies, emitted at the second harmonic (Figure 8). The details of how we obtain the lightcurves

from our code are given in Appendix C. We have assumed that $B_0 = 4$ kG, $\alpha = 46°5$, $\beta = 76°$, and $n_{p0} = 10^9$ cm^{-3}. We have also assumed a Gaussian profile for the ECME pulses (Section C) with $\sigma_\theta = 3°$ (this corresponds to a FWHM of $\approx 7°$). The values of the flux densities at a given frequency are normalized by the maximum value at that frequency. We also show normalized $B_{\rm LoS}$ in Figure 8. For convenience, we name the magnetic null, at which $B_{\rm LoS}$ changes from negative to positive, as null 1 and the other magnetic null, where $B_{\rm LoS}$ changes from positive to negative, as null 2. We find that near null 1, the pulse from the south magnetic hemisphere (blue curve) arrives ahead of those from the north magnetic hemisphere (red curve), and vice versa. Note that this characteristic was also obtained in Leto et al. (2016), in which (effectively) the single refraction scenario was used. We also find that the separation between pulses around a given null decreases as we go to higher frequencies. This frequency-dependent separation
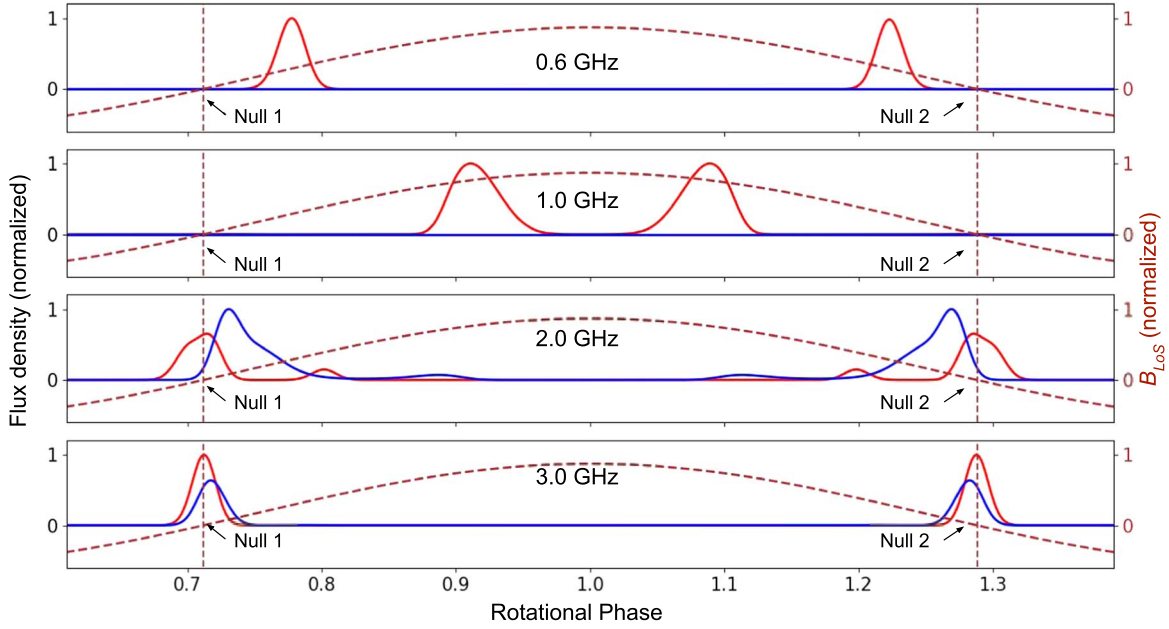
Figure 10. Normalized lightcurves obtained for the IM density profile given by Equation (9), with $\sigma_\theta = 3°$. The red and blue lines correspond to ECMEs produced at the north and south magnetic hemispheres, respectively. The brown dashed curves correspond to the normalized LoS magnetic field.

is a strong function of density in the IM. The proposed framework will be useful for exploiting this dependence to estimate density in the IM.

4.2. ECME from a Star with an Azimuthally Asymmetric Magnetosphere

Stars with high obliquity are predicted to have overdense regions in their magnetosphere, which are not azimuthally symmetric (the "Rigidly Rotating Model," or "RRM"; Townsend & Owocki 2005). The deviation from the azimuthal symmetry is most severe for β close to 90°. Among the stars known to produce ECME, many have high obliquities, e.g., the magnetic B star HD 142990 has $\beta \approx 84°$ (Shultz et al. 2019). In this section, we carry out our simulation to ascertain the effect of this azimuthally asymmetric density distribution on the ECME properties of the star over a wide range of frequencies.

The density profile that we will take as an example is inspired from the RRM model of Townsend & Owocki (2005), and is given by the following equation:

$$n_p = \frac{n_{p0}}{r}\left(1 + 100\exp\left(-\frac{3\tilde{z}^2}{\sigma(\tilde{x})^2}\right)(1 - \Delta)\right)$$

$$\tilde{z} = r\sin(\theta - \theta_0), \quad \tilde{x} = r\cos(\theta - \theta_0)$$

$$\theta_0 = \frac{\pi}{2}(1 + \sin\phi_B), \quad \sigma(\tilde{x}) = 0.7\exp\left(\frac{R_A}{R_A + \tilde{x}^2}\right)$$

$$\Delta(r) = \frac{1}{1 + \exp\{2M(r - r_0)\}}, \quad r_0 = 2.5. \quad (9)$$

Note that the equations are written for the magnetic frame of reference. This density profile is shown in Figure 9 for two values of ϕ_B: 0° and 30°.

We again consider ECME at 0.6, 1, 2, and 3 GHz, emitted at the X-mode, in the second harmonic. In Figure 10, we show the normalized output lightcurves along with B_{LoS} (brown dashed curve) for $\sigma_\theta = 3°$. These lightcurves are different from those

in Figure 8, or those simulated by Leto et al. (2016), in many important aspects:

1. At 0.6 and 1 GHz, there is no pulse from the south magnetic hemisphere.
2. Between 0.6 and 1 GHz, the offset of the pulse from the magnetic null is higher at higher frequencies, unlike the case for the azimuthally symmetric IM (Section 4.1, Figure 8).
3. At 2 and 3 GHz, the strengths of the pulses from the north and the south magnetic hemispheres are different despite the fact that we considered a perfectly dipolar magnetic field.
4. At 2 GHz, there are weaker secondary pulses, in addition to the primary pulse.
5. The sequence of arrival of pulses at 2 and 3 GHz from the opposite magnetic hemispheres are the opposite of what would be expected for the azimuthally symmetric case (Figure 8).
6. The magnetic null phases do not lie at the midpoint between the pulses from the opposite magnetic hemispheres.

We first address the last point, which is straightforward to understand. Due to the asymmetry of the magnetosphere, the radiation produced at the north and the south magnetic hemispheres will undergo different amounts of deviation, resulting in a loss of symmetry about the magnetic null.

The reason an ECME pulse is absent from south magnetic hemisphere at 0.6 and 1 GHz is that for the density distribution considered here, many of the rays produced at the relevant auroral circles cannot pass through the IM because of the very high density for which the refractive index becomes imaginary. This happens for the rays originating at the south magnetic hemispheres. Note that an order of magnitude estimate of the critical density, above which radiation at 0.6 and 1 GHz cannot pass, is $5 \times 10^9\,\text{cm}^{-3}$ and $10^{10}\,\text{cm}^{-3}$, respectively, which is achievable for the density profile given by Equation (9).
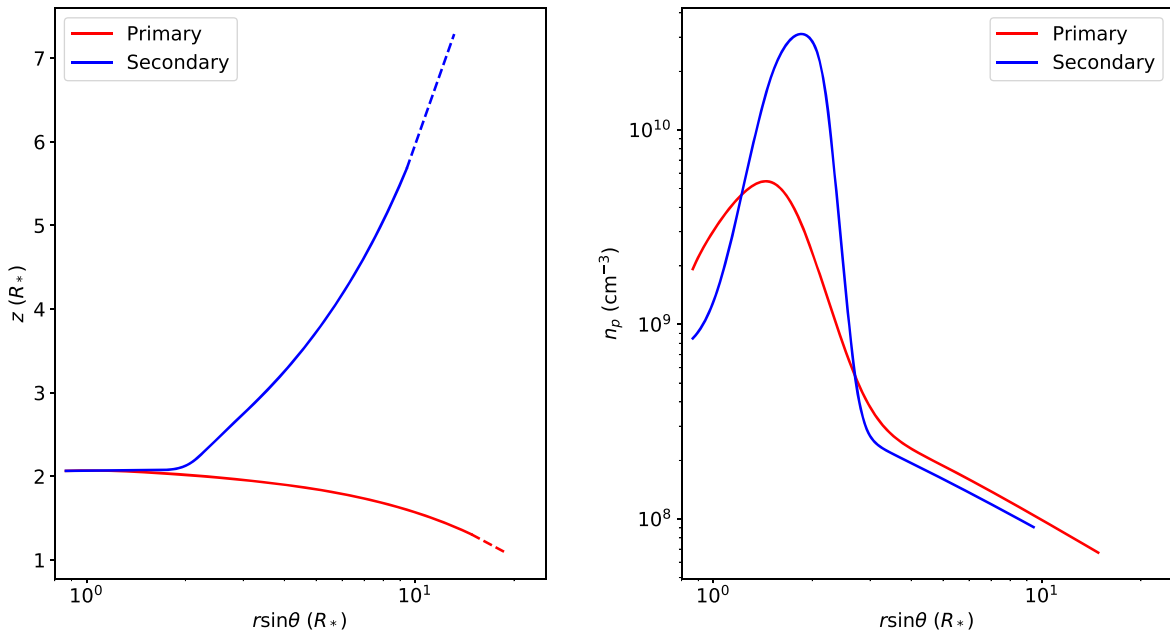
Figure 11. Left: the ray paths that contribute to the 2 GHz pulse (*X*-mode) from the north magnetic hemisphere for an azimuthally asymmetric density distribution. The red and blue lines correspond to the primary and secondary components of the pulse, respectively (Figure 10; for details, see Section 4.2). Right: the corresponding number densities along the paths inside IM.

The higher offset of ECME pulses from the magnetic null at higher frequencies between 0.6 and 1 GHz is due to the fact that the density experienced by ECME at 1 GHz is much higher than that for 0.6 GHz.

The third point about the different pulse strengths for pulses from the north and south magnetic hemispheres is actually not surprising. In our framework the strength of an ECME pulse is determined by three factors: (1) the number of rays that contribute to the pulse, (2) the difference in deviations suffered by the contributing rays, and (3) the angles made by the contributing rays with the line of sight (LoS) at their closest proximities. The larger the number of contributing rays, and smaller the angle between the contributing rays and the LoS at their closest encounters, the higher the corresponding pulse strength. On the other hand, the larger the difference in deviations suffered, the lower the pulse height and the broader the pulse, since the contributing rays reach the observer over a relatively large range of rotational phases. For the density distribution that we have considered, these three factors need not be the same for pulses from opposite magnetic hemispheres, or at different frequencies, resulting in the discrepancies mentioned above. However, an additional factor causing ECMEs of different strengths at different magnetic hemispheres is the instability at the emission site (e.g., Trigilio et al. 2011; B. Das et al. 2020, in preparation). Thus the different strengths of ECME pulses do not give much insight for extracting information on the density in the magnetosphere.

The existence of weaker secondaries at a particular frequency (here at 2 GHz) is also a consequence of the three factors (described in the preceding paragraph) assuming different values for different frequencies and different magnetic hemispheres. To illustrate the difference in ray paths, in the left panel of Figure 11 we show one of the contributing rays to the primary and one contributing to the secondary pulse from the north magnetic hemisphere at 2 GHz. We also show the corresponding densities encountered along the ray paths in the right panel. We further find that the number of contributing

rays to the secondary is smaller than that for the primary, which is expected from observations, as the latter is much stronger than the former.

Finally, the most important way in which the refraction in the IM can affect the ECME lightcurve is to alter the sequence of arrival of pulses around the magnetic nulls. As mentioned in the introduction (Section 1), we expect that when the north magnetic pole of the star is approaching and the south magnetic pole is receding (i.e., B_{LoS} is changing from negative to positive, the rotational phases around null 1), the pulse from the south magnetic hemisphere will arrive before the pulse from the north magnetic hemisphere, and vice versa. This expectation is based on the assumption that radiation produced at the north magnetic hemisphere always gets deviated upward and that at the south magnetic hemispheres gets deviated downward (e.g., see Figure 2 of Leto et al. 2016). While this assumption holds for the density profile considered in Section 4.1, or for a constant density medium like the one considered in the "single refraction model," it need not be valid for the density profile given by Equation (9). For example, we show paths followed by some of the rays that contribute to the observable pulses at 3 GHz in the left panel of Figure 12, and the corresponding densities along the ray path in the right panel. We find that the radiation from the south magnetic hemisphere undergoes significant deviation upward (instead of downward). For the case of the north magnetic hemisphere, some of the rays get deviated slightly upward and the rest deviate downward. The net result is that we see an opposite sequence of arrival of pulses near the magnetic nulls.

In reality, we often see ECME pulses not behaving ideally in terms of pulse shapes, their phases of arrival, etc. For example, Das et al. (2019a) observed a double-peaked ECME pulse from HD 142990 for which there is not yet any satisfactory explanation. For such cases, we can use a realistic model for the magnetosphere and try to find out whether any such nonideality can be obtained from the propagation effect. This in
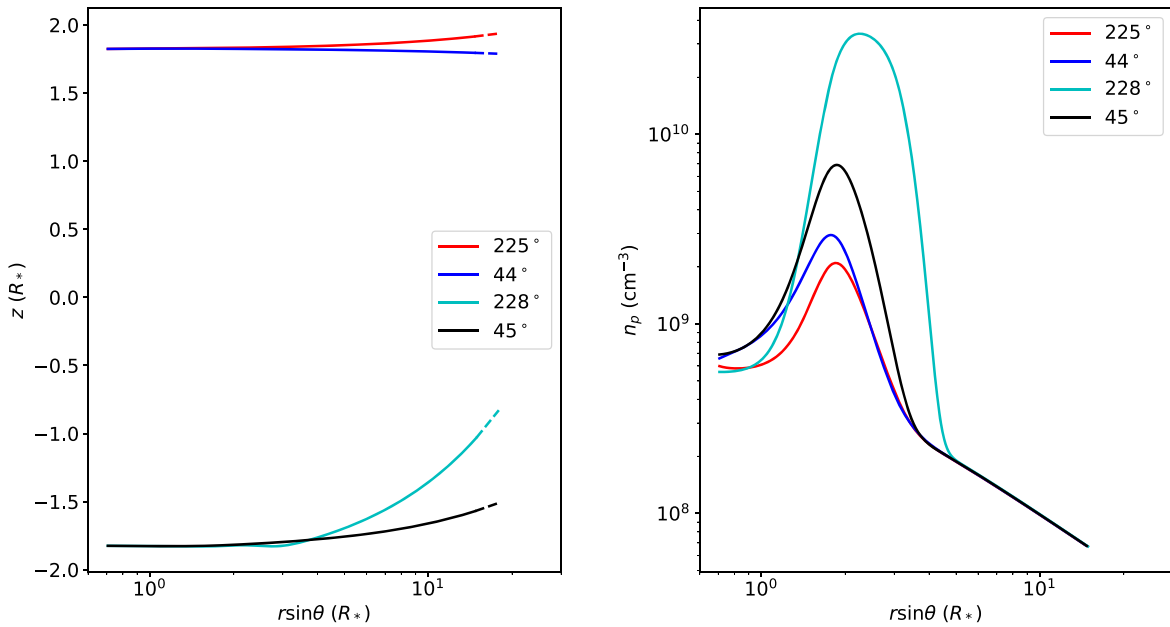
Figure 12. Left: the ray paths corresponding to the different ranges of magnetic azimuthal coordinates ϕ_B that contribute to the observable pulses at 3 GHz (*X*-mode). The legends show the values of ϕ_B of the contributing auroral points. Right: the number density experienced along the ray paths inside the IM.

turn will allow us to get a better idea of the density structure in the stellar magnetosphere.

5. Discussion

The ECME observed from hot magnetic stars can become a highly useful tool to probe their magnetospheres. Since different frequencies arise at different heights, they pass through different parts of the IM and can undergo significantly different deviations depending on the density distribution they encounter in the IM. Such a situation is more likely for a star with high obliquity. In that case, if the type of density distribution is known (e.g., from the RRM model), we can use the framework presented here to simulate multifrequency lightcurves. By comparing these lightcurves with the observed ones, one can obtain the best-fit values for different parameters associated with the density distribution. While doing so, one must discard the assumption of density discontinuities at the IM boundary and work with a density grid instead. The latter strategy can be easily incorporated in the current code. This framework can also be useful for disentangling effects produced by a complex magnetic field and those due to propagation effect. Until now, various nonideal properties observed in the ECME lightcurves, such as offset from the magnetic nulls, absence of pulse at a particular circular polarization, etc., have been attributed to the presence of a magnetic field more complex than a dipole (e.g., Trigilio et al. 2000; Das et al. 2019a; Leto et al. 2019). Here we show that even for an ideal dipolar magnetic field, the ECME lightcurve can be highly nonintuitive. To disentangle these effects from those produced by a complex magnetic field, multifrequency observations will be instrumental.

Although this framework is general enough to work for a magnetic field more complex than a dipole, we have currently implemented only the dipole case in our code. We plan to generalize it in the future. We emphasize that this framework

will enable the scientific community to understand the "nonideal" properties of ECME, and in the process of doing so, will let us probe the density structure in the magnetosphere of the host star.

Appendix A
Formulae for Refractive Indices

The refractive indices μ for the *X* and *O* modes are given by (Lee et al. 2013)

$$\mu_X^2 = 1 - \frac{\nu_p^2}{\nu(\nu + \tau\nu_B)},$$

$$\mu_O^2 = 1 - \frac{\tau\nu_p^2}{\nu(\tau\nu - \nu_B \cos^2\psi)}. \qquad (A1)$$

Here ψ is the angle between the wavevector and the local magnetic field, ν_p and ν_B are the local plasma frequency and the electron cyclotron frequency, respectively, and τ is

given by

$$\tau = (\sigma + \sqrt{\sigma^2 + \cos^2 \psi}) \frac{\nu_p^2 - \nu^2}{|\nu_p^2 - \nu^2|},$$

$$\sigma = \frac{\nu \nu_B \sin^2 \psi}{2|\nu^2 - \nu_p^2|}.$$

Appendix B
Rotation Matrices for Going from the Line-of-sight Frame of Reference to That of the Magnetic Field

In order to obtain the lightcurve, we will have to define the three frames of reference, namely, the reference frame of the magnetic field, the reference frame of the rotation axis and the reference frame of the LoS. In the magnetic frame of reference, we have already taken the Z-axis to lie along the dipole axis; in the rotation frame, the Z-axis lies along the rotation axis, and in the LoS frame, the Z-axis lies along the LoS. We first write the rotation matrix for getting the components of a vector X in the star's rotation frame from the known components in the LoS frame. Let the inclination angle be α and the obliquity be β. We choose the LoS to lie in the YZ plane of the rotation frame as shown in Figure B1.

From Figure B1, we get

$$X_{\text{rot}} = \begin{pmatrix} 1 & 0 & 0 \\ 0 & \cos\alpha & -\sin\alpha \\ 0 & \sin\alpha & \cos\alpha \end{pmatrix} X_{\text{LoS}}. \qquad (B1)$$

The above relation allows us to go from the LoS frame of reference to the star's rotation frame of reference. Next we have to find the rotation matrix for going from the rotation to the magnetic frame of reference. We define the zero of the rotational phases in such a way that the LoS, rotation axis, and magnetic axis lie in the same plane (Figure B2). We will find the rotation matrix between the magnetic and rotation frame for any rotational phase in two steps. In the first step, we take $\beta = 0$ and the other two axes in one frame are misaligned with their counterparts in the other frame by an angle ϕ_{rot} (rotational phase is $\phi_{\text{rot}}/2\pi$). This is shown in the left panel of Figure B3. We denote the axes in this "intermediate magnetic frame" as X_{B1}, Y_{B1}, and Z_{B1}.

From the left panel of Figure B3, we get

$$X_{B1} = \begin{pmatrix} \cos\phi_{\text{rot}} & \sin\phi_{\text{rot}} & 0 \\ -\sin\phi_{\text{rot}} & \cos\phi_{\text{rot}} & 0 \\ 0 & 0 & 1 \end{pmatrix} X_{\text{rot}}.$$

In the second step, we consider the rotation matrix between this intermediate frame and the real magnetic frame. From the right panel of Figure B3, we have

$$X_B = \begin{pmatrix} 1 & 0 & 0 \\ 0 & \cos\beta & \sin\beta \\ 0 & -\sin\beta & \cos\beta \end{pmatrix} X_{B1}$$

$$= \begin{pmatrix} \cos\phi_{\text{rot}} & \sin\phi_{\text{rot}} & 0 \\ -\cos\beta \sin\phi_{\text{rot}} & \cos\beta \cos\phi_{\text{rot}} & \sin\beta \\ \sin\beta \sin\phi_{\text{rot}} & -\sin\beta \cos\phi_{\text{rot}} & \cos\beta \end{pmatrix} X_{\text{rot}}. \qquad (B2)$$

Substituting from Equation (B1) in Equation (B2), we get the rotation matrix for going from the LoS to the magnetic frame of
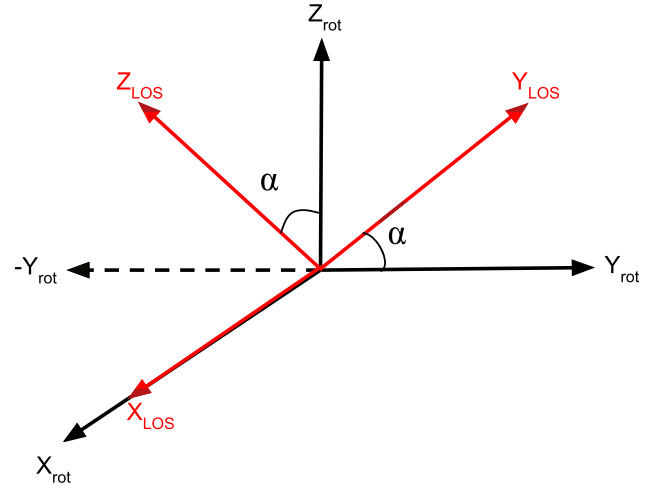

Figure B1. The relation between the LoS and rotational frame of reference. The X-axes of both frames are aligned. The Z-axis of the rotation frame is along the rotation axis and that in the case of the LoS frame is along the LoS. The LoS lies in the $-YZ$ plane of the rotational frame and is inclined by an angle α w.r.t. the rotation axis. The rotation matrix is given by Equation (B1).
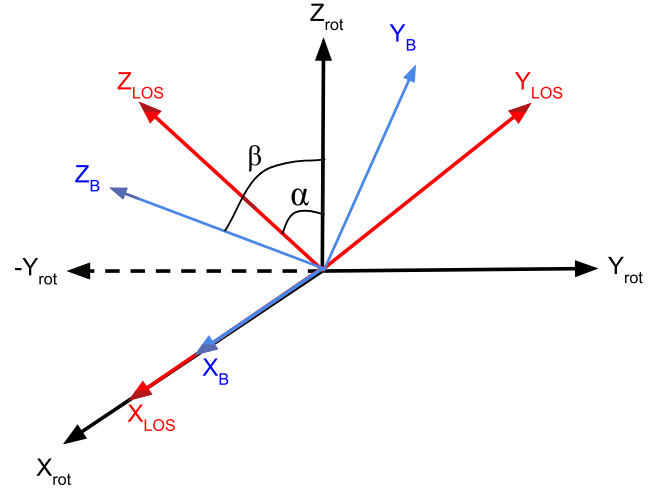

Figure B2. The relation among the LoS, rotation, and magnetic frames of reference when the rotational phase is zero. At this phase, the LoS, rotation axis, and the magnetic dipole axes lie in the same plane and the X-axes of respective frames of reference are aligned. The magnetic axis makes an angle of β w.r.t. the rotation axis and the angle between the LoS and the magnetic dipole axis is $|\beta - \alpha|$ at this rotational phase.

reference, which is

$$\begin{pmatrix} \cos\phi_{\text{rot}} & \cos\alpha \sin\phi_{\text{rot}} & -\sin\alpha \sin\phi_{\text{rot}} \\ -\cos\beta \sin\phi_{\text{rot}} & \cos\alpha \cos\beta \cos\phi_{\text{rot}} & -\sin\alpha \cos\beta \cos\phi_{\text{rot}} \\ & +\sin\alpha \sin\beta & +\cos\alpha \sin\beta \\ \sin\beta \sin\phi_{\text{rot}} & -\cos\alpha \sin\beta \cos\phi_{\text{rot}} & \sin\alpha \sin\beta \cos\phi_{\text{rot}} \\ & +\sin\alpha \cos\beta & +\cos\alpha \cos\beta \end{pmatrix}. \qquad (B3)$$

Using this matrix, we can write the LoS vector in the magnetic frame of reference (LoS_B) for a given rotational phase $\phi_{\text{rot}}/2\pi$.
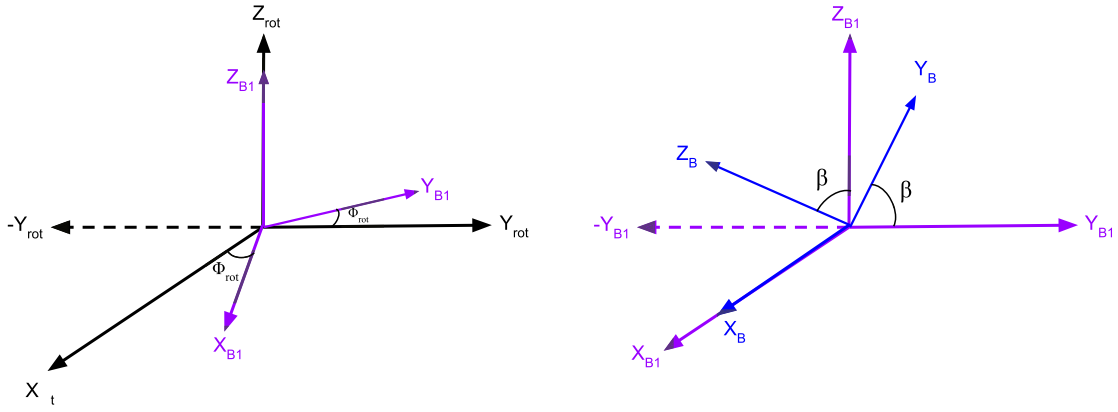
Figure B3. The relation between the magnetic and rotation frame for a given rotational phase $\phi_{\rm rot}/2\pi$. We can get this relation by first considering the figure on the left panel, where we have the the Z-axes of frames aligned for both frames (B_1 frame, $\beta = 0$, and the other two are inclined by an angle of $\phi_{\rm rot}$. We next consider the relation between this intermediate B_1 frame and the magnetic frame (right panel), where now the X-axes are aligned and the other two are inclined by an angle β. The rotation matrix is given by Equation (B2).

Appendix C
Lightcurves of ECME for a Given Density Profile in the IM

The lightcurves at a given frequency can be obtained by the following steps:

1. Obtain $k_{\rm out}$ vectors for the full auroral circles (near both magnetic hemispheres). The auroral circles are defined by the frequency of ECME, harmonic number, and the magnetic field strength (Section 3).
2. For each rotational phase, obtain the components of the LoS vector in the magnetic frame of reference (Equation (B3)).
3. For that rotational phase, calculate the angle θ_k, which is the angle between the LoS vector and a given $k_{\rm out}$.
4. Add a contribution of $\exp(-\theta_k^2/\sigma_\theta^2)$ to the lightcurve for that rotational phase, where σ_θ is a measure of the ECME beamwidth.
5. Repeat step 2 to step 4 for each rotational phase.

ORCID iDs

Barnali Das ● https://orcid.org/0000-0001-8704-1822
Surajit Mondal ● https://orcid.org/0000-0002-2325-5298
Poonam Chandra ● https://orcid.org/0000-0002-0844-6563

References

Andre, P., Montmerle, T., Feigelson, E. D., Stine, P. C., & Klein, K.-L. 1988, ApJ, 335, 940
Das, B., Chandra, P., Shultz, M. E., & Wade, G. A. 2019a, ApJ, 877, 123
Das, B., Chandra, P., Shultz, M. E., & Wade, G. A. 2019b, MNRAS, 489, L102
Das, B., Chandra, P., & Wade, G. A. 2018, MNRAS, 474, L61
Hallinan, G., Antonova, A., Doyle, J. G., et al. 2006, ApJ, 653, 690
Hallinan, G., Antonova, A., Doyle, J. G., et al. 2008, ApJ, 684, 644
Kochukhov, O., Lüftinger, T., Neiner, C., Alecian, E. & MiMeS Collaboration 2014, A&A, 565, A83
Lee, S.-Y., Yi, S., Lim, D., et al. 2013, JGRA, 118, 7036
Leto, P., Trigilio, C., Buemi, C. S., et al. 2016, MNRAS, 459, 1159
Leto, P., Trigilio, C., Buemi, C. S., Umana, G., & Leone, F. 2006, A&A, 458, 831
Leto, P., Trigilio, C., Oskinova, L. M., et al. 2019, MNRAS, 482, L4
Lo, K. K., Bray, J. D., Hobbs, G., et al. 2012, MNRAS, 421, 3316
Shultz, M. E., Wade, G. A., Rivinius, T., et al. 2019, MNRAS, 490, 274
Townsend, R. H. D., & Owocki, S. P. 2005, MNRAS, 357, 251
Townsend, R. H. D., Owocki, S. P., & Ud-Doula, A. 2007, MNRAS, 382, 139
Trigilio, C., Leto, P., Leone, F., Umana, G., & Buemi, C. 2000, A&A, 362, 281
Trigilio, C., Leto, P., Umana, G., Buemi, C. S., & Leone, F. 2008, MNRAS, 384, 1437
Trigilio, C., Leto, P., Umana, G., Buemi, C. S., & Leone, F. 2011, ApJL, 739, L10
Trigilio, C., Leto, P., Umana, G., Leone, F., & Buemi, C. S. 2004, A&A, 418, 593
Ud-Doula, A., Owocki, S. P., & Townsend, R. H. D. 2008, MNRAS, 385, 97
ud-Doula, A., Sundqvist, J. O., Owocki, S. P., Petit, V., & Townsend, R. H. D. 2013, MNRAS, 428, 2723
Wolin, S. 1953, JOSA, 43, 373
Zarka, P. 1998, JGR, 103, 20159